ADVANCED MATERIALS INTERFACES
www.advmatinterfaces.de

Constructing a "Pizza-Like" MoS_2/Polypyrrole/Polyaniline Ternary Architecture with High Energy Density and Superior Cycling Stability for Supercapacitors

Kai Wang, Le Li, Ying Liu, Chao Zhang, and Tianxi Liu**

Polypyrrole (PPy) and polyaniline (PANI) are most promising candidates for high energy and power density supercapacitors. However, their relative low surface area and poor cyclic stability greatly limit their practical applications. Morphology- and size-controlled micro/nanostructure formation of such materials may lead to enhanced performance. Here, the solvent-exchange method is proposed for the preparation of high-concentration few-layer MoS_2 (f-MoS_2) suspension in an ethanol–water mixed solvent. PPy layers with high surface coverage are formed on the resultant dispersible f-MoS_2 by in situ polymerization of pyrrole. The MoS_2/PPy hybrid is then used as the reactive layer for subsequent in situ growth and attachment of PANI, thus forming a "pizza-like" MoS_2/PPy/PANI ternary nanostructure. The rational design of such hierarchical nanostructures greatly enhances the specific capacitance up to 1273 F g^{-1} at 0.5 A g^{-1} and effectively improves the cyclic performance maintaining ≈83% after 3000 charge/discharge cycles. The excellent performances of MoS_2/PPy/PANI hybrid are mainly attributed to robust interconnected frameworks for improved electrical conductivity and well-defined porosities for enhanced electrolyte/electrode interaction. The superior electrochemical performance thus suggests a promising strategy for fabricating component adjustable, high energy density, and durable nanostructures as novel electrode materials for supercapacitors.

1. Introduction

Efficient and environmentally friendly energy conversation has become major hurdles for a wide utilization of renewable energy resources around the world. Among the various energy storage systems, the supercapacitors are considered as the most promising candidates due to their low cost, environmental friendliness, high power density, and excellent cycling stability.[1–5] There are two main subdivisions derived from different charge storage mechanism in supercapacitors: (a) the ion adsorption and desorption (also called electrical double layer capacitance, EDLC) where the capacitance is derived from the charge separation at the electrode/electrolyte interface, and (b) the reversible faradaic reaction where the pseudocapacitance arises from reversible faradic reaction occurring at the electrode/electrolyte interface.[6–8] Among various electrode materials, conducting polymers such as polypyrrole (PPy) and polyaniline (PANI),[9–11] are receiving specific attentions due to their intrinsic characteristics including low cost, easy preparation, remarkable storage capacity, good conductivity, and broad voltage window.[12–15] Basically, the utilization of conducting polymers as electrode materials usually shows a considerable enhancement in specific energy density, but those electrodes may exhibits a poor cycling stability due to serious volumetric swelling and shrinking of conducting polymers during cycles.[16–19]

An emerging solution to overcome the challenges facing conducting polymers including poor electroactive stability and weak mechanical properties is to grow conducting polymers on the surfaces of various supporting materials such as graphene, metal oxides, metal dichalcogenide, etc.[20–25] The superiority of using those supporting materials is evident because they can offer a uniform and large-surface-area substrate to immobilize conducting polymers for efficient energy storage.[26,27] Molybdenum disulfide (MoS_2) is a typical 2D layered transition metal dichalcogenide which possesses unique structure features with large interlayer distance of 1.24 Å, high electrochemical activity, and good chemical stability. Therefore, MoS_2 has become a particularly promising candidate for applications in supercapacitors[28–30] and lithium ion batteries.[31–33] Meanwhile, the weak van der Waals interaction and relative large interlayer distance between MoS_2 layers facilitates the intercalation of positive ions (H^+, K^+, and Li^+), resulting in enlarged effective surface area which could be used as a 2D template for growing conducting polymers or other functional nanoparticles.[34–40]

Herein, we developed a simple and efficient strategy to construct MoS_2/PPy/PANI ternary hybrids via two successive polymerizations of PPy and PANI on few-layer MoS_2 (f-MoS_2) templates. Surprisingly, a rational design of such ternary nanocomposites enables greatly improved specific capacitance as

K. Wang, L. Li, Y. Liu, Prof. C. Zhang, Prof. T. X. Liu
State Key Laboratory for Modification of Chemical Fibers and Polymer Materials &
College of Materials Science and Engineering
Donghua University
Shanghai 201620, P. R. China
E-mail: czhang@dhu.edu.cn; txliu@fudan.edu.cn

DOI: 10.1002/admi.201600665

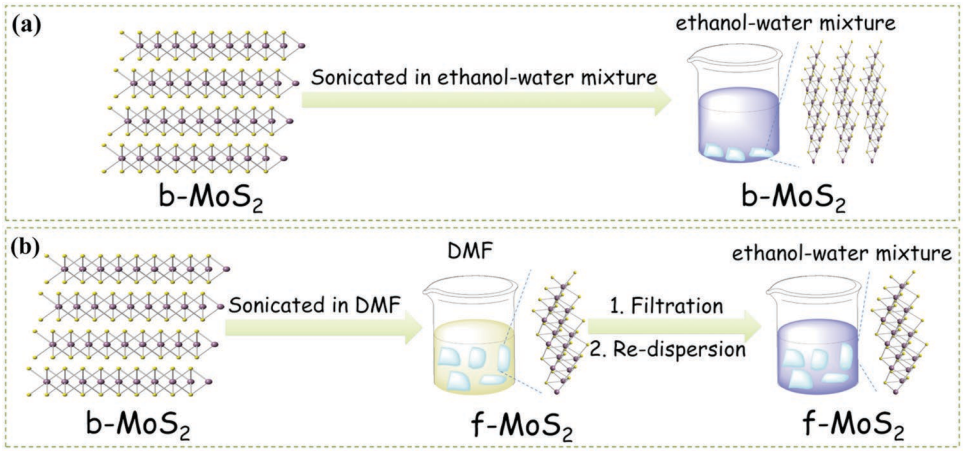

Figure 1. Schematic of solvent-exchange method for the exfoliation and dispersion of f-MoS_2.

well as significantly enhanced cycling stability. It is expected that the present work could provide a new strategy to design and prepare conducting polymer-based hybrids and widen their applications as promising electrode materials in energy storage systems, particularly in supercapacitors.

2. Results and Discussion

Herein we developed a versatile and scalable solvent-exchange strategy for liquid exfoliation and dispersion of f-MoS_2 nanosheets in low-boiling solvents, such as ethanol and water, which can be easily utilized in further applications. As demonstrated in **Figure 1**a, a long time (even longer than 10 h) sonication of b-MoS_2 in an ethanol–water mixed solvent can hardly result in a successful exfoliation of b-MoS_2 into f-MoS_2. By choosing appropriate solvents, a uniform suspension of high-concentration f-MoS_2 with a majority of single and fewer layers can be obtained by direct exfoliation of b-MoS_2 powder via an ultrasound exfoliation in certain solvents such as *N*,*N*-dimethyl formamide (DMF) and 1-methyl-2-pyrrolidinone (NMP).[41]

Mechanism for the efficient liquid phase exfoliation of b-MoS_2 in DMF was carefully investigated. On the one hand, shear forces and cavitations during a bath sonication, i.e., the expansion and collapse of micrometer-sized bubbles or voids in liquids because of the pressure fluctuations, might induce an exfoliation of bulk layered materials.[42] The hydrodynamic forces derived from increased pressure and temperature during the bath sonication process give rise to the breakdown of b-MoS_2 into smaller fragments and thinner layers in solvents. After that, the continuous sonication leads to the cleavage of layers into ultrathin sheets by overcoming the van der Waals attractions between the adjacent layers. On the other hand, in the view of thermodynamic theories, the lower the differences of surface energies between solvents and 2D materials, the better the exfoliation process should be.[43] DMF, with surface energy of ≈70 mJ m^{-2} which is close to 70–75 mJ m^{-2} of 2D MoS_2, is expected to achieve an excellent exfoliation of MoS_2.[44]

As shown in Figure 1b, by simply sonicating the wet f-MoS_2 sediment in an ethanol–water mixed solvent, the f-MoS_2 was successfully transferred into the ethanol–water mixture from DMF. As shown in Figure S1 of the Supporting Information, the dispersion of f-MoS_2 in an ethanol–water mixed solvent was stable after standing for two weeks, indicating the good exfoliation and dispersion of f-MoS_2 in the mixed solvent. In order to prevent the restackings of f-MoS_2, the interactions between the chosen solvents and f-MoS_2 need to offset the interlayer attractive forces between f-MoS_2. Previous findings pointed out that chemically dissimilar 2D materials such as MoS_2 could be well dispersed in solvents that have similar surface tensions with MoS_2.[44,45] Considering the surface tension of DI water (72 mN m^{-1}) and ethanol (22.1 mN m^{-1}), the ethanol–water mixture can match the optimized value for the dispersion of MoS_2 (40 mN m^{-1}). The solvent-exchange process thus establishes a new paradigm in the formation and dispersion of f-MoS_2 nanosheets in low-boiling solvents, and the utilization of environmentally friendly and inexpensive ethanol–water mixtures as solvents will be favorable in the fabrication of f-MoS_2 based composite materials for various applications. Figure S2 of the Supporting Information gives the field-emission scanning electron microscopy (FESEM) images of b-MoS_2 and f-MoS_2, respectively. Upon exfoliation, f-MoS_2 exhibit uniform and exfoliated layered nanostructures with typical lateral sizes of several hundred nanometers (Figure S2b, Supporting Information), which are much smaller than those of b-MoS_2 (Figure S2a, Supporting Information). The transmission electron microscopy (TEM) observations of f-MoS_2 sample at different magnifications (Figure S3, Supporting Information) further indicate the morphology of f-MoS_2 nanosheets are composed of single and fewer layers. Figure S4a of the Supporting Information exhibits the tapping mode AFM image of the f-MoS_2. The f-MoS_2 nanosheets are several micrometers in width. Smaller fragments were also observed on the surface of big-sized MoS_2 nanosheets, which were consistent with previous TEM results. The height profile of AFM image suggests that the thickness of the f-MoS_2 is below ≈10 nm (Figure S4b, Supporting Information). Given that the thickness of the monolayer MoS_2 is ≈1 nm and the interlamellar spacing value of f-MoS_2 (002) plane is 0.62 nm, respectively, the AFM results suggest that the as-prepared f-MoS_2 contains less than six layers.

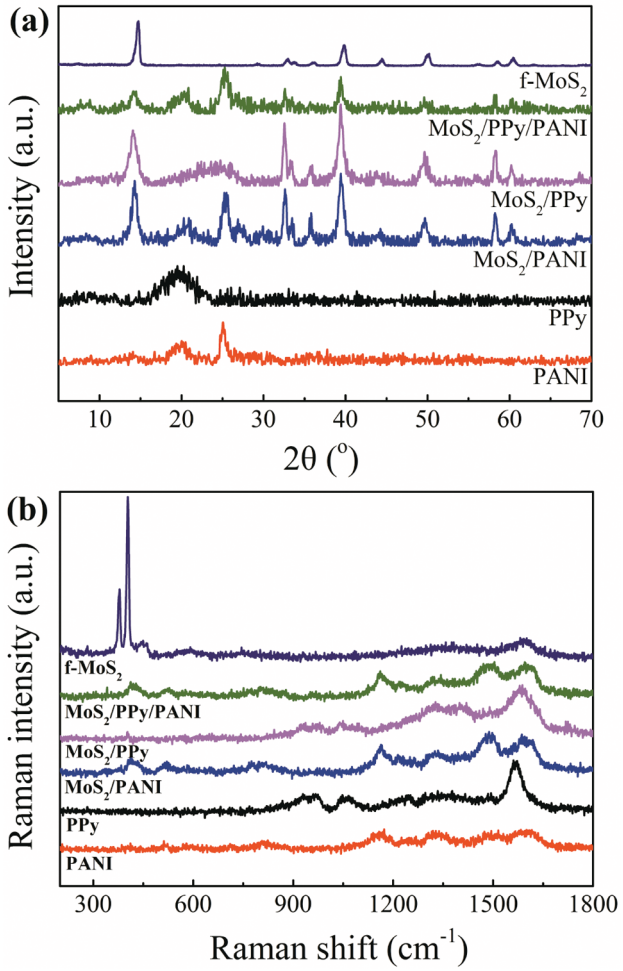

Figure 2. a) XRD patterns and b) Raman spectra of f-MoS_2, PPy, PANI, MoS_2/PPy, MoS_2/PANI, and MoS_2/PPy/PANI.

Figure 2a shows X-ray diffraction (XRD) patterns of f-MoS_2, PPy, PANI, MoS_2/PPy, MoS_2/PANI, and MoS_2/PPy/PANI, respectively. The f-MoS_2 exhibits the diffraction peaks centered at 2θ = 14.7°, 32.8°, 33.7°, 36.2°, 39.9°, 44.4°, 50.1°, 56.1°, 58.6°, and 60.5°, respectively, which can be assigned to the (002), (100), (101), (102), (103), (006), (105), (106), (110), and (008) planes of 2H-phase MoS_2, respectively. The f-MoS_2 shows a broadened primary (002) diffraction peak compared with that of b-MoS_2 (Figure S5, Supporting Information), indicating that more defects might be introduced into the f-MoS_2 with decreased nanometer-scale sizes.[46,47] Neat PPy shows a typical broad and weak reflection located in the range of 2θ = 15°–25°, which is assigned to the characteristic peak of amorphous PPy. For neat PANI, the crystalline peaks appear at 2θ = 15.3°, 20.7°, and 25.2°, respectively, corresponding to (011), (020), and (200) crystal planes of PANI in its emeraldine salt form, respectively.[48] Moreover, the weak diffraction peak at 2θ = 20.5° for PANI is observed, suggesting PANI is in a semicrystalline state in the hybrid.[49] For the MoS_2/PPy/PANI ternary hybrid, the XRD pattern validates that the PPy and PANI are successfully attached onto f-MoS_2 templates.

Raman spectroscopy technique might give more structure information for the hybridization of MoS_2 and conducting polymers, and therefore the Raman spectra of the related samples are tested and shown in Figure 2b and Figure S6 of the Supporting Information. For the Raman pattern of b-MoS_2 (Figure S6, Supporting Information), there are two strong signals at 375.6 and 403.1 cm^{-1}, respectively, corresponding to the in-plane E^1_{2g} and out-of-plane A_{1g} vibration modes, respectively. Remarkably, the Raman pattern of f-MoS_2 indicates that both E^1_{2g} and A_{1g} vibrations red-shift and soften after the exfoliation of b-MoS_2 into f-MoS_2. The peak difference between E^1_{2g} and A_{1g} was 27.5 and 25.2 cm^{-1} for b-MoS_2 and f-MoS_2, respectively, indicating that f-MoS_2 nanosheets are thinner than the bulk ones after efficient exfoliation.[50–52] Besides, the line widths (5–6 cm^{-1}) for the f-MoS_2 are larger than the reported data (2–5 cm^{-1}) of mechanically exfoliated MoS_2 single crystals,[53] which is attributed to a smaller crystallite size and a large amount of defects of the resultant f-MoS_2.[54] For neat PANI, the peaks are observed situated at 416, 514, 807, 1161, 1217, 1326, 1492, and 1597 cm^{-1}, respectively, which are ascribed to out-of-plane C—H wag, out-of-plane C—N—C torsion, imine deformation, in-plane C—H bending, in-plane ring deformation, C–$N^{\bullet+}$ stretching, C=N stretching of quinoid, C—C stretching of benzoid, respectively.[55,56] For neat PPy sample, two weak peaks centered at 929 and 970 cm^{-1}, respectively, are associated with the quinoid polaronic and bipolaronic structure, respectively. The broad peak obtained near 1046 cm^{-1} corresponds to the C—H in-plane deformation.[57,58] The appearance of peaks near 1564 and 1334 cm^{-1} is attributed to the π conjugated structure and ring stretching mode of the polymer backbone, respectively.[59] Hence, Raman spectra clearly indicate the presence of PPy and PANI in the hybrid samples.

As demonstrated in **Figure 3**a, when the pyrrole monomer was added into the f-MoS_2 suspension in an ethanol–water mixed solvent during in situ polymerization of PPy, it might be adsorbed onto the surface of f-MoS_2 due to the electrostatic interaction between negatively charged MoS_2 and positively charged pyrrole.[60] Upon the addition of ammonium persulphate (APS), thin PPy films were polymerized and attached onto the surface of f-MoS_2. Likewise, when the aniline monomer was added into the MoS_2/PPy suspension in solvents, aniline can be adsorbed on the surface of MoS_2/PPy substrate due to certain interaction forces such as van der Waals interaction, cohesive forces between aniline and PPy-coated f-MoS_2. In both of the two in situ polymerization systems, it is noted that sulfuric acid serves as a dopant for both conducting polymers. The morphology and microstructure of the MoS_2/PPy/PANI samples were further investigated by SEM and TEM observations. As shown in Figure S7a of the Supporting Information, different from an irregular sphere-like structure for neat PPy, we can see that among the MoS_2/PPy (Figure S7c, Supporting Information) and MoS_2/PPy/PANI (Figure 3b,c), the PPy in a planar shape is closely coated on the surface of 2D f-MoS_2. Different from randomly connected fiber-like structure for neat PANI (Figure S7b, Supporting Information), MoS_2/PPy hybrid as supporting materials might supply a large number of active sites for the nucleation of PANI, thus resulting in homogeneous coating of PANI nanosized particles on the surfaces of MoS_2/PPy. In comparison with the MoS_2/PANI

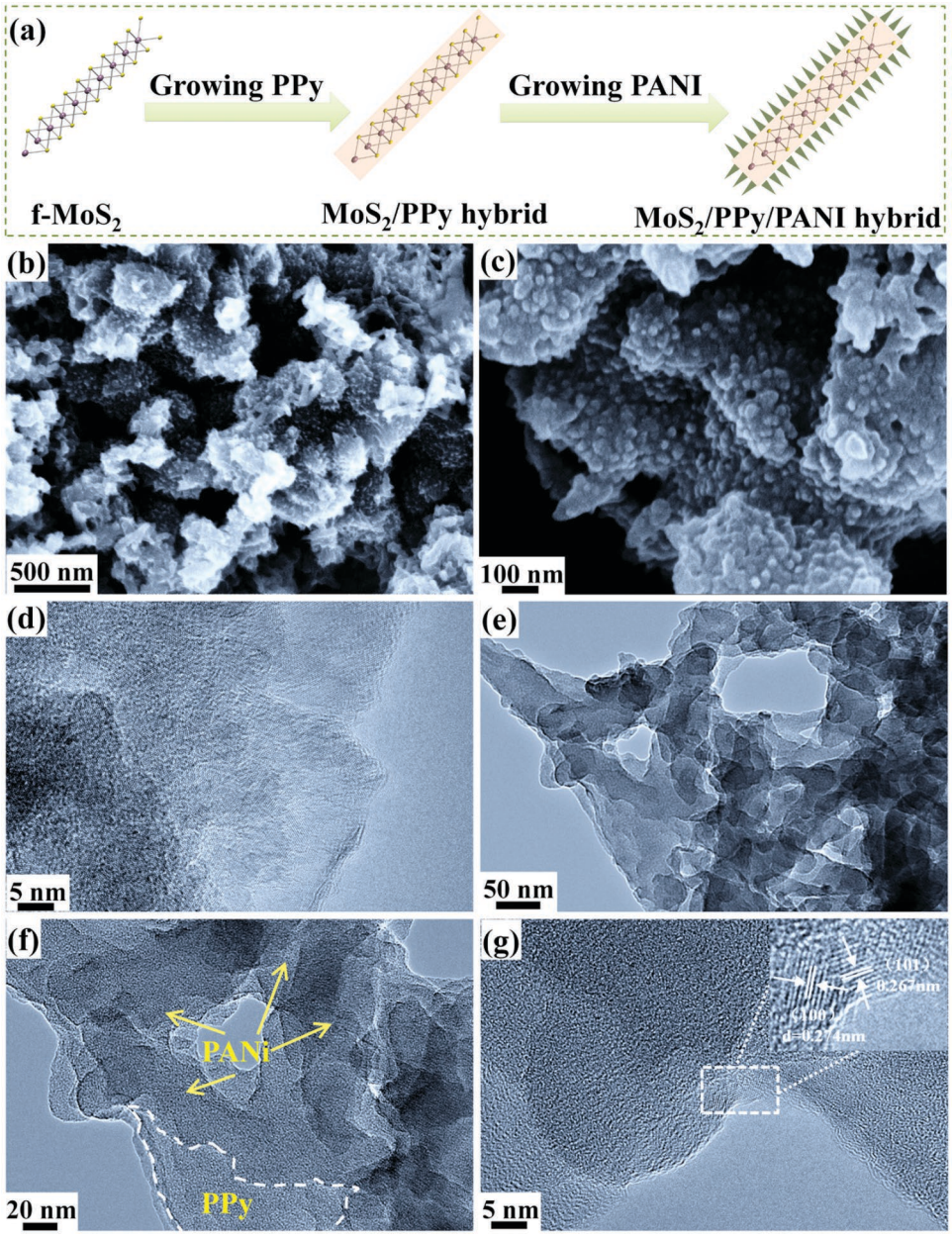

Figure 3. a) Schematic illustration of the synthetic process for the formation of the MoS_2/PPy/PANI hybrid. SEM images of b,c) MoS_2/PPy/PANI at low and high magnifications, respectively. TEM images of d) f-MoS_2, and e–g) MoS_2/PPy/PANI at different magnifications.

in Figure S7d of the Supporting Information, the PANI particles with smaller sizes in the MoS_2/PPy/PANI hybrid show a better dispersion. Such particular structure of the MoS_2/PPy/PANI ternary hybrid could increase the dispersion of PANI and improve the interfaces of PANI with electrolyte, which might be beneficial for the improvement of electrochemical performance of MoS_2/PPy/PANI as electrode materials. The PANI nanoparticles allow the effective intercalation of H^+ ions into both its frameworks and interlayers of MoS_2 thin nanosheets, which served as ions reservoir for energy storage and shorten the diffusion paths of transportation of electrons.[35] Furthermore, intercalation of H^+ improve the conductivity of conducting polymer. As shown in Figure 3d, f-MoS_2 demonstrates an ultrathin sheet-like nanostructure with well-defined edges. Figure 3e–g is typical TEM images of MoS_2/PPy/PANI ternary hybrid, indicating the f-MoS_2 nanosheets are uniformly surrounded by conducting polymers. The growth of ultrathin PPy layers on f-MoS_2 nanosheets is further recognized by TEM observations, as marked in the white irregular dashed lines in Figure 3f, while uniform decoration of particle-like PANI on f-MoS_2 nanosheets can be explicitly observed (marked by yellow arrows in Figure 3f), showing the successful formation of the expected designed "pizza-like" nanostructures of MoS_2/PPy/PANI ternary hybrid. Moreover, the selected area of MoS_2 lamella within the MoS_2/PPy/PANI ternary hybrid was further studied by the high-resolution TEM observations in Figure 3g,

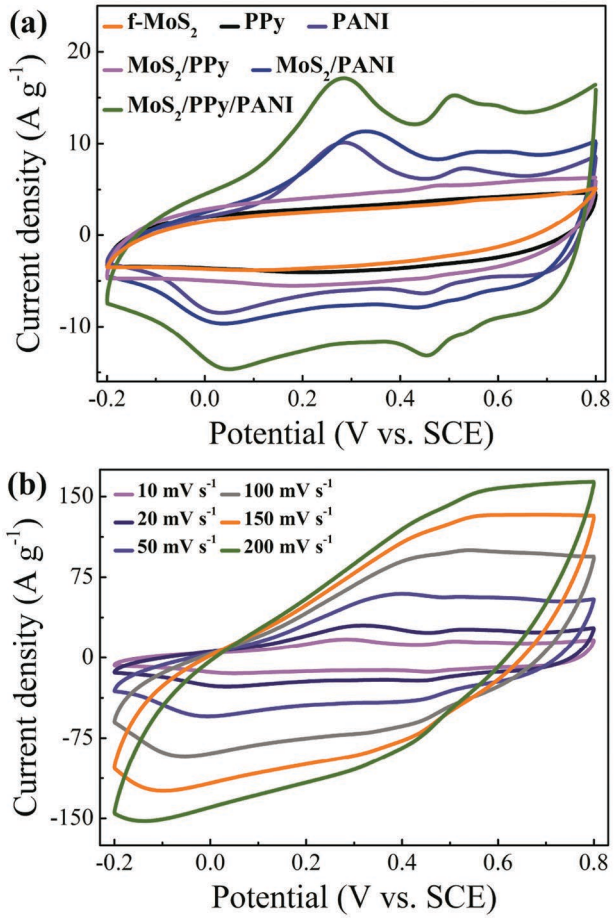

Figure 4. a) Comparison of CV curves of f-MoS_2, PPy, PANI, MoS_2/PPy, MoS_2/PANI, and MoS_2/PPy/PANI at a scan rate of 10 mV s^{-1}. b) CV curves of MoS_2/PPy/PANI composite at various scan rates of 10, 20, 50, 100, 150, and 200 mV s^{-1}, respectively.

showing some fringes with a lattice distance of 0.274 and 0.267 nm which are attributed to the (100) and (101) planes of hexagonal MoS_2 crystalline structure, respectively. Other areas of the amorphous material layer without fringes, actually, are the closely attached PPy layers on f-MoS_2 template.

Cyclic voltammetry (CV) and galvanostatic charge/discharge measurements were performed to evaluate the electrochemical performance of the MoS_2/PPy/PANI electrodes. **Figure 4**a exhibits the CV curves of f-MoS_2, PPy, PANI, MoS_2/PPy, MoS_2/PANI, and MoS_2/PPy/PANI electrodes at a scan rate of 10 mV s^{-1} in a 0.5 M H_2SO_4 solution electrolyte, revealing that the MoS_2/PPy/PANI electrode exhibits the best electrochemical performance among all the samples. The CV curve of f-MoS_2 electrode shows a rectangular shape without obvious redox peaks, indicating an ideal electric double-layer capacitive behavior and desirable fast charge/discharge properties for the 2D MoS_2 materials.[12] The CV curves of PPy and MoS_2/PPy electrodes exhibit similar rectangular shapes indicating capacitive-like responses among PPy and MoS_2/PPy electrodes. PANI electrode shows two separate couples of redox peaks in the scan area, which are attributed to the transition of PANI from the semiconducting-state (leucoemeraldine) to the conductive form (emeraldine), and the transition from emeraldine to the pernigraniline, respectively. The MoS_2/PPy/PANI electrode shows similar redox peaks with those of PANI and MoS_2/PANI electrodes, but exhibits enlarged surrounded area compared with those of f-MoS_2, PPy, PANI, MoS_2/PPy, and MoS_2/PANI at the same scan rate, indicating that the specific capacitance of MoS_2/PPy/PANI electrode is larger than those of neat conducting polymers or MoS_2/conducting polymer binary hybrid electrodes. These results indicate a synergistic effect from the contributions from the combinations of MoS_2, PPy, and PANI. Figure 4b presents the CV curves of the MoS_2/PPy/PANI electrode over scan rates from 10 to 200 mV s^{-1} with a potential window between −0.2 and 0.8 V. An obvious increase of current density with scan rate was observed, and a nearly rectangular shape with a mirror-image feature at high scan rate up to 200 mV s^{-1} indicates a good rate capability for the MoS_2/PPy/PANI electrode.

The galvanostatic charge/discharge plots for all the electrodes measured at a current density of 1 A g^{-1} are shown in **Figure 5**a. The MoS_2/PPy/PANI electrode exhibits a significantly higher specific capacitance than those of individual conducting polymers or MoS_2/conducting polymer binary hybrid. Typical galvanostatic charge/discharge curves of MoS_2/PPy/PANI electrode under different current densities are presented in Figure 5b. All the curves are not ideal straight lines, indicating a faradic reaction occurs during charge/discharge process. In addition, there is no obvious IR drop even at a high discharge current density of 20 A g^{-1} caused by equivalent series resistance (R_s), suggesting a favorable capacitive characteristic with a fast current–voltage responding to the MoS_2/PPy/PANI electrode materials. The discharge specific capacitance (C_m) can be calculated as follows:

$$C_m = \frac{I \cdot \Delta t}{m \cdot \Delta V} \quad (1)$$

where C_m is specific capacitance, I is charge/discharge current, Δt is the discharge time, ΔV is 1 V, and m is the mass of the active material in the electrode. By means of calculations from the discharge time of galvanostatic charge/discharge curves of all samples at various current densities, the relationships of specific capacitances as a function of current densities for all the samples were calculated and shown in Figure 5c. The specific capacitances of MoS_2/PPy/PANI electrode are much higher than those of MoS_2, PPy, and PANI at the same current density. The MoS_2/PPy/PANI electrode exhibits an enhanced specific capacitance of 1273 F g^{-1} at a current density of 0.5 A g^{-1}, which is much higher than those of f-MoS_2 (169 F g^{-1}), PPy (136 F g^{-1}), PANI (528 F g^{-1}), MoS_2/PPy (449.5 F g^{-1}), and PANI/PANI (784 F g^{-1}). Besides, the coulombic efficiency of the MoS_2/PPy/PANI electrode is observed above 92% at 1 A g^{-1}, indicating a good electrochemical reversibility. The MoS_2/PPy/PANI electrode remains as high as 673 F g^{-1} at a high current density of 10 A g^{-1}, maintaining ≈53% of its capacitance at a current density of 0.5 A g^{-1}. The excellent rate capability in the MoS_2/PPy/PANI electrode could be attributed to short ion diffusion paths and good electrical conductivities. The large improvement in specific capacitances for the MoS_2/PPy/PANI electrode might be attributed to a synergistic effect between PPy and PANI.[61]

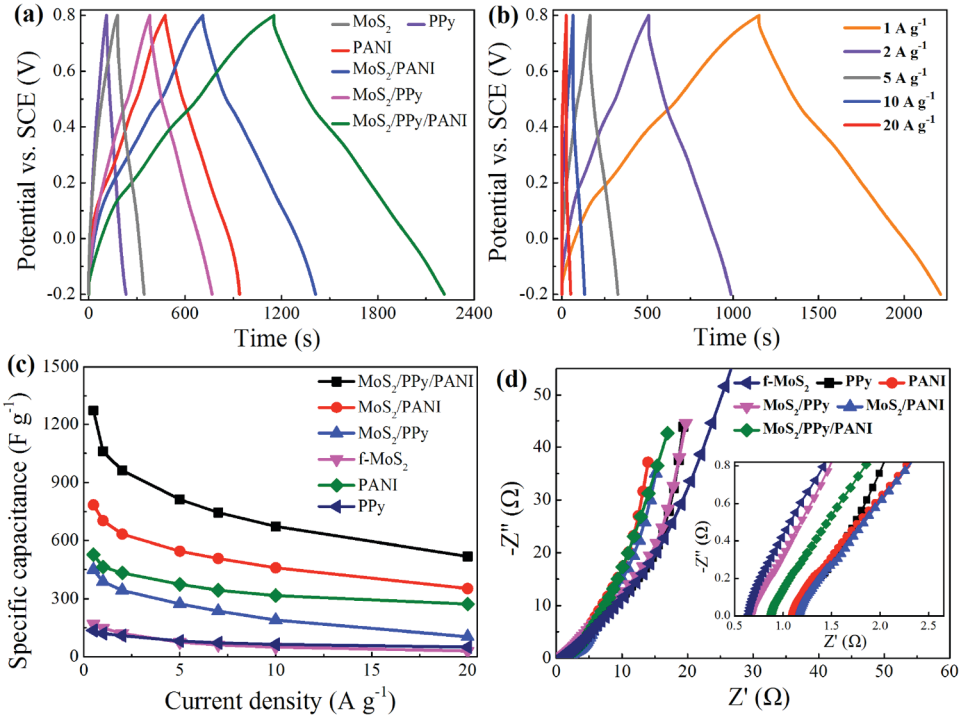

Figure 5. a) Comparison of galvanostatic charge/discharge curves of f-MoS_2, PPy, PANI, MoS_2/PPy, MoS_2/PANI, and MoS_2/PPy/PANI at a current density of 1 A g^{-1}. b) Galvanostatic charge/discharge curves of MoS_2/PPy/PANI at different current densities. c) Specific capacitances of f-MoS_2, PPy, PANI, MoS_2/PPy, MoS_2/PANI, and MoS_2/PPy/PANI at various current densities. d) Comparison of Nyquist plots of electrodes of f-MoS_2, PPy, PANI, MoS_2/PPy, MoS_2/PANI, and MoS_2/PPy/PANI in the frequency range of 1 MHz to 0.01 Hz (inset is the enlargement of the high-frequency region).

The intimately attached PANI nanoparticles on the layered PPy structures might exhibit enhanced electrode/electrolyte interface interactions, providing more electroactive regions with rapid, reversible faradic reactions and shorter ion diffusion paths.[62] In addition, MoS_2 nanosheets in the ternary hybrid might provide a large surface area that allows excellent electrolyte access as well as providing a low internal resistance.[63–65] Furthermore, the transition metal centers of MoS_2 might form strong coordinations with nitrogen atoms in PANI and PPy. The Mo ions from MoS_2 which are intimately coordinated with nitrogen atoms (from conducting polymer) possess a range of oxidation states from +2 to +6, resulting in an additional pseudocapacitance performance.

Electrochemical impedance spectroscopy (EIS) tests were utilized to describe the electrochemical process of the electrode/electrolyte interface. The Nyquist plots of electrodes obtained by EIS measurements are displayed in Figure 5d. There are no semicircles for all the electrodes in high-frequency regions, indicating extremely low electron transfer resistances of all electrodes. Nearly straight lines in low frequency regions represent the ion diffusion and transport due to an EDLC behavior. The R_s is determined by taking the high frequency intercept on the X-axis, which is decided by the combination of intrinsic resistance of substrate, ionic resistance of electrolyte, and contact resistance at the electrode/current collector interface. Among them, the R_s of the MoS_2/PPy/PANI electrode is larger than f-MoS_2 and MoS_2/PPy, and this phenomenon might be ascribed to the hierarchical structures which constrain the movement of ions among the MoS_2/PPy/PANI electrode. The above results also indicate that the homogenous PPy ultrathin layers on MoS_2 nanosheets are of great priority to provide supporting substrates for the efficient immobilization of PANI nanoparticles.[12]

Cycling stability is another important criterion for the real applications of supercapacitors. Cycling performance for an assembled symmetric supercapacitor using the MoS_2/PPy/PANI electrodes as both anode and cathode at a working potential window from 0 to 1.0 V was evaluated at a current density of 2 A g^{-1} for 3000 cycles, as shown in **Figure 6**a. Generally, using individual conducting polymers or MoS_2/conducting polymer binary hybrid as electrode materials can hardly achieve a satisfying cyclic stability, but a rational combination of the MoS_2/PPy/PANI ternary hybrid can reach significant enhancement of cycling stability. For example, neat conducting polymer electrodes show a fast decay during cycles, namely, with capacitance retention of 46% for neat PPy and 43% for neat PANI, respectively, after 3000 charge/discharge cycles. When the PPy and PANI were grown on f-MoS_2 separately, a barely satisfactory cycling stability with a capacitance retention of 62% for MoS_2/PPy and 69% for MoS_2/PANI, respectively, was observed. Specifically, for the "pizza-like" hierarchical nanostructures of the MoS_2/PPy/PANI, the capacitance retention maintains 83% after 3000 cycles. The good cycling stability for the MoS_2/PPy/PANI electrode over MoS_2/PANI electrode might be ascribed to the existence of intermediate layer of PPy between f-MoS_2 nanosheets and PANI nanoparticles, which buffers the volumetric swelling and shrinking during the charge/discharge process.[30,66] The EIS measurements were further carried out

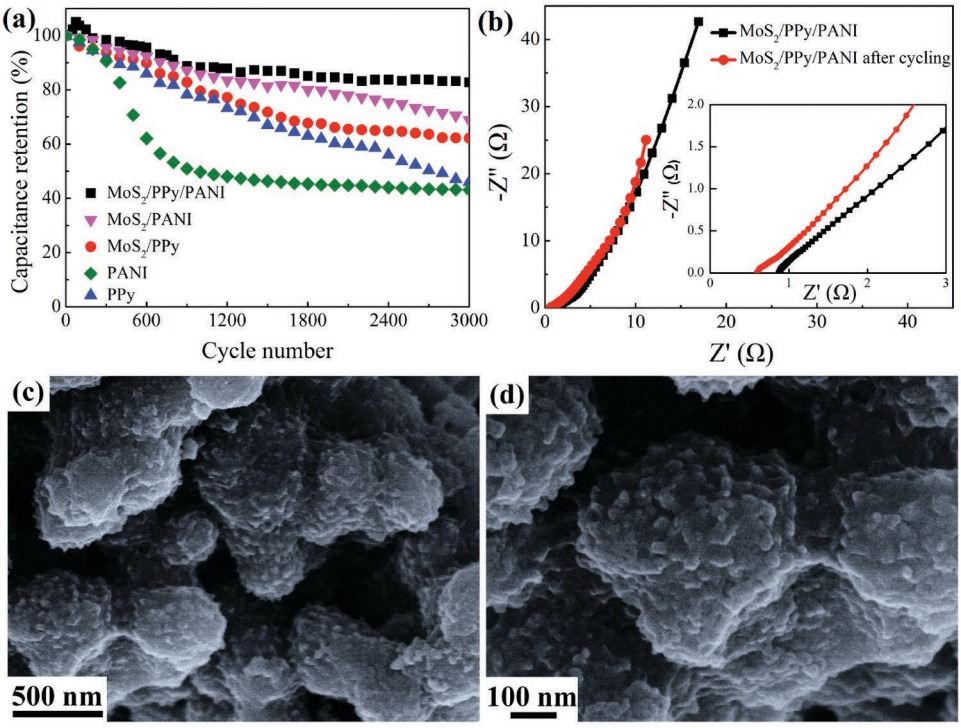

Figure 6. a) Cyclic stability of PPy, PANI, MoS_2/PPy, MoS_2/PANI, and MoS_2/PPy/PANI for 3000 charge/discharge cycles. b) Comparison of Nyquist plots of MoS_2/PPy/PANI electrode before and after cycling (inset is the enlargement of the high-frequency region). c,d) SEM images of the MoS_2/PPy/PANI electrode after 3000 cycles at different magnifications.

to investigate the electrochemical behavior of the PPy, PANI, MoS_2/PPy, MoS_2/PANI, and MoS_2/PPy/PANI electrodes after 3000 charge and discharge cycles (Figure 6b and Figure S8, Supporting Information). It can be seen that R_s of the MoS_2/PPy/PANI electrode become lower even after a long-term cycling test, indicating the fast electron transport through conducting polymers to the current collector and the excellent structure stability of the "pizza-like" architecture during cycling. For comparison, the R_s of the PPy, PANI, MoS_2/PPy, and MoS_2/PANI electrodes increased in varying degrees. In particularly, there exists a semicircle in the plot of PANI electrode which diameter represents the charge-transfer resistance (R_{ct}), indicating the microstructure of electrode might have been broken down during cycles. The EIS results thus imply the easy penetration of electrolytes into the electrodes, and the structure stability with favorable conductivities.

To further study the mechanism for enhanced cyclic stability of the ternary hybrid electrode materials, the structural evolution in the MoS_2/PPy/PANI electrode after 3000 cycles was characterized by SEM. As shown in Figure 6c,d, the "pizza-like"MoS_2/PPy/PANI architecture still remains the original architecture, and no significant aggregation and collapse are observed after cycling. Typically, PANI nanoparticles still uniformly support on the surface of MoS_2/PPy with a nanosize of ≈20 nm, and little crumble can be observed. At the same time, although the intercalation of H^+ ions into interlayers of MoS_2 might cause the structure instability, no obvious structure changes in MoS_2/PPy substrate are observed due to the closely surrounded PPy nanolayers on f-MoS_2, which weaken the restacking of f-MoS_2 into aggregates during cycles. Such good maintenance of the microstructure might be the underlying factor for the largely enhanced cycling stability in the MoS_2/PPy/PANI electrode.[67] The excellent capacitance retention for the MoS_2/PPy/PANI electrode can be also attributed to the MoS_2 nanosheets providing a 2D nanostructure for the efficient immobilization of two kinds of conducting polymers, and the unique "pizza-like" PPy-PANI nanostructures on the MoS_2 thus postpones the crumpling and agglomeration of conducting polymers into a denser structure during cycles. Stable maintenance of the microstructure derived from the strong interface interaction between PPy and MoS_2 layers should be another potential factor for the enhanced cycling stability. MoS_2 substrate provides large specific surface area, and can accommodate large volumetric expansion due to repeated structure pulverization of conducting polymers during charge/discharge process, and thus improves the stability of the conducting polymer.[68–71] Therefore, the above-mentioned synergistic effect and optimized nanostructure between MoS_2 and PPy, PANI, and PPy corporately facilitates the resultant MoS_2/PPy/PANI owning high specific capacitance, good rate capability, and excellent long-term cycle stability.

3. Conclusions

In summary, a ternary nanocomposite of 2D MoS_2, PPy, and PANI with a "pizza-like" hierarchical nanostructure was designed and constructed. Among the MoS_2/PPy/PANI hybrid, ultrathin PPy layer is intimately attached to f-MoS_2 nanosheets thus forming a MoS_2/PPy core–shell nanostructure, and PANI

nanoparticles are separately assembled on the surface of pie-like MoS_2/PPy hybrid. Remarkably, the favorable nanostructure of MoS_2/PPy/PANI ternary hybrid might utilize the excellent pseudocapacitive behavior of PPy/PANI and the unique 2D structure of MoS_2, thus efficiently avoiding the structural pulverization during charge/discharge procedures. On the one hand, 2D MoS_2 was utilized as active materials providing more tracks for the insertion and extraction of ions in the electrochemical process. In addition, MoS_2 also offered a uniform and large-surface-area platform to immobilize conducting polymers because transition metal centers of MoS_2 can form strong coordination with nitrogen atoms in PPy. On the other hand, the unique structure and close interaction between PPy and PANI prevents the polymers from severely swelling and shrinking during cycles. The excellent electrochemical performance indicates that the "pizza-like" nanostructure possesses a synergistic effect of PPy and PANI, which shows improved capacitance and superior stability than individual components or binary composites (MoS_2/PPy or MoS_2/PANI). Excellent capacitance and supreme cycling life of such ternary hybrid suggests a highly prospective application as high-performance electrode materials for supercapacitors.

4. Experimental Section

Materials: Bulk MoS_2 (b-MoS_2, ≈ 325 mesh) was purchased from Alfa Aesar. Pyrrole (AR grade) and aniline (AR grade) were purchased from Sigma-Aldrich and purified by distillation before use. DMF, ethanol, sulfuric acid, and APS were supplied from Sinopharm Chemical Regent and used as received. Deionized (DI) water was used throughout the experiments.

Preparation of f-MoS_2: Homogeneous dispersion of f-MoS_2 nanosheets in an ethanol–water mixed solvent was achieved by solvent-exchange method. First, the exfoliation of b-MoS_2 in DMF into f-MoS_2 nanosheets was achieved by a bath sonication, as reported elsewhere.[41,72,73] In a typical process, 1.0 g b-MoS_2 powder was added into 100 mL of DMF followed by a sonication for 3 h. After the sonication, the suspension was centrifuged at 1500 rpm for 30 min and the sediment was discarded to remove unexfoliated or thick MoS_2 flakes, and then f-MoS_2 was gathered by a filtration of the supernatants. After filtration, the resultant solid was washed with ethanol for several times and collected on the membrane. To obtain a homogeneous suspension of f-MoS_2 in an ethanol–water mixed solvent, the wet exfoliated f-MoS_2 sediment is redispersed in the corresponding solvent followed by a bath sonication for 5 min, thus giving a uniform suspension of f-MoS_2 nanosheets in an ethanol–water (3/1 v/v) mixed solvent. The final concentration of f-MoS_2 in the mixed solvent was determined by a weighting method. Typically, we took at least 50 mL of MoS_2 dispersion in the ethanol–water mixed solvent, and then weighed the dried solids to calculate the solid content. In contrast, it is basically impossible to directly exfoliate the dried f-MoS_2 sediment or b-MoS_2 in the ethanol–water mixed solvent even after a long-time sonication.

Preparation of MoS_2/PPy/PANI Ternary Hybrid: MoS_2/PPy/PANI ternary hybrid was prepared by two successive polymerizations of pyrrole and aniline on the f-MoS_2 templates. In a typical process, 20 mg of f-MoS_2 was dispersed in a mixed solvent of 30 mL absolute ethanol and 10 mL 1 M H_2SO_4 under sonication at ambient temperature. Then the suspension was transferred into an ice bath, and cooled down to 0 ± 2 °C. After stirring for 30 min, 0.194 g (200 µL) of pyrrole was added into the suspension. After stirring for 10 min, 20 mL of APS solution (16.5 mg mL^{-1} in 1 M H_2SO_4 solution) was added into the above suspension, and the mole ratio of pyrrole monomer to APS was guaranteed to be 2/1. The polymerization process was carried out in an ice-bath for 12 h with vigorous stirring. Then, the suspension was filtered and rinsed several times with DI water and ethanol successively, and then the resultant solid was vacuum-dried at 60 °C for 24 h to obtain the MoS_2/PPy hybrid. Furthermore, 232.9 mg of aniline monomer was suspended in 30 mL suspension (solvent: 10 mL 1 M H_2SO_4 and 20 mL ethanol) containing 30 mg of MoS_2/PPy, sonicated for 30 min, and then cooled to 0 ± 2 °C. After 10 min, 10 mL of APS solution (22.8 mg mL^{-1} in 1 M H_2SO_4 solution) was added into the above suspension, and the mole ratio of aniline monomer to APS was guaranteed to be 2/1. The polymerization was carried out at 0 ± 2 °C for 12 h with vigorous stirring. Then, the suspension was filtered and rinsed several times with DI water and ethanol successively, and then vacuum-dried at 60 °C for 24 h to obtain the MoS_2/PPy/PANI ternary hybrid. For comparison, neat PPy, neat PANI, and MoS_2/PANI hybrids were synthesized under the same conditions.

Characterization: The morphology of the samples was evaluated by FESEM (Ultra 55) and TEM (Tecnai G2 20 TWIN). XRD patterns were obtained by an X'Pert Pro X-ray diffractometer with Cu K_α radiation (λ = 0.1542 nm) at a current of 40 mA and voltage of 40 kV. Raman spectra were recorded on a Renishaw in plus laser Raman spectrometer with λ_{exc} = 532 nm. AFM (NanoScope V, Bruker, USA) was utilized to test the f-MoS_2 in typical tapping mode.

Electrochemical Characterization: The capacitive behaviors for the samples were measured with a CHI 660D electrochemical workstation using a standard three-electrode setup. The working electrodes were prepared by mixing 80 wt% active materials, 10 wt% carbon black (Super P), and 10 wt% polyvinylidene fluoride (PVDF) in NMP solution, followed by drying it on a graphite paper current collector (1 × 1 cm^2) in vacuum at 80 °C overnight. The typical loading density for the resultant electrode is ≈1.5–2.0 mg cm^{-2}. A platinum wire and SCE was used as the counter electrode and the reference electrode, respectively, and a 0.5 M H_2SO_4 aqueous solution was used as the electrolyte. CV measures were performed within a potential range of –0.2–0.8 V versus SCE at scan rates of 10–200 mV s^{-1}. Galvanostatic charge/discharge testing was done from –0.2 to 0.8 V versus SCE at a current density of 0.5, 1, 2, 5, 7, 10, and 20 A g^{-1}, respectively. EIS was performed in the frequency range from 0.01 to 10^6 Hz at open-circuit potential with an AC voltage amplitude of 5 mV.

Supporting Information

Supporting Information is available from the Wiley Online Library or from the author.

Acknowledgements

This work was supported by the National Natural Science Foundation of China (Nos. 21504012, 51125011, and 51433001) and the Fundamental Research Funds for the Central Universities of China (No. 16D110617).

Received: July 12, 2016
Published online:

[1] Y. M. Chen, Z. Li, X. W. D. Lou, *Angew. Chem. Int. Ed.* **2015**, *127*, 10667.
[2] L. Yu, B. Guan, W. Xiao, X. W. D. Lou, *Adv. Energy Mater.* **2015**, *5*, 1500981.
[3] P. Simon, Y. Gogotsi, *Nat. Mater.* **2008**, *7*, 845.
[4] C. Zhong, Y. Deng, W. Hu, J. Qiao, L. Zhang, J. Zhang, *Chem. Soc. Rev.* **2015**, *44*, 7484.
[5] T.-Y. Dai, R. Tang, X.-X. Yue, L. Xu, *Chin. J. Polym. Sci.* **2015**, *33*, 1018.

[6] V. Gupta, N. Miura, *Electrochim. Acta* **2006**, *52*, 1721.
[7] B. E. Conway, *Electrochemical Supercapacitors: Scientific Fundamentals and Technological Applications*, Springer Science & Business Media, New York **2013**.
[8] X. Y. Yu, L. Yu, H. B. Wu, X. W. D. Lou, *Angew. Chem. Int. Ed.* **2015**, *54*, 5331.
[9] Q. Qu, Y. Zhu, X. Gao, Y. Wu, *Adv. Energy Mater.* **2012**, *2*, 950.
[10] H. Zhang, Z. Hu, M. Li, L. Hu, S. Jiao, *J. Mater. Chem.* **2014**, *2*, 17024.
[11] B. Anothumakkool, R. Soni, S. N. Bhange, S. Kurungot, *Energy Environ. Sci.* **2015**, *8*, 1339.
[12] H. Tang, J. Wang, H. Yin, H. Zhao, D. Wang, Z. Tang, *Adv. Mater.* **2015**, *27*, 1117.
[13] J. Wang, Z. Wu, K. Hu, X. Chen, H. Yin, *J. Alloys Compd.* **2015**, *619*, 38.
[14] G. Wang, L. Zhang, J. Zhang, *Chem. Soc. Rev.* **2012**, *41*, 797.
[15] G. A. Snook, P. Kao, A. S. Best, *J. Power Sources* **2011**, *196*, 1.
[16] W. Zhao, S. Wang, C. Wang, S. Wu, W. Xu, M. Zou, A. Ouyang, A. Cao, Y. Li, *Nanoscale* **2016**, *8*, 626.
[17] G. Yu, X. Xie, L. Pan, Z. Bao, Y. Cui, *Nano Energy* **2013**, *2*, 213.
[18] Y. Huang, J. Tao, W. Meng, M. Zhu, Y. Huang, Y. Fu, Y. Gao, C. Zhi, *Nano Energy* **2015**, *11*, 518.
[19] G. Garberoglio, *Chem. Phys. Lett.* **2009**, *467*, 270.
[20] J. Ni, G. Wang, J. Yang, D. Gao, J. Chen, L. Gao, Y. Li, *J. Power Sources* **2014**, *247*, 90.
[21] D. Gao, Z. Zhang, L. Ding, J. Yang, Y. Li, *Nano Res.* **2015**, *8*, 546.
[22] J. Yan, Q. Wang, T. Wei, Z. Fan, *Adv. Energy Mater.* **2014**, *4*, 1300816.
[23] H. Tang, H. Yin, J. Wang, N. Yang, D. Wang, Z. Tang, *Angew. Chem. Int. Ed.* **2013**, *125*, 5695.
[24] Y. Zhao, J. Liu, Y. Hu, H. Cheng, C. Hu, C. Jiang, L. Jiang, A. Cao, L. Qu, *Adv. Mater.* **2013**, *25*, 591.
[25] S. Zhao, Y. Li, H. Yin, Z. Liu, E. Luan, F. Zhao, Z. Tang, S. Liu, *Sci. Adv.* **2015**, *1*, 1500372.
[26] G. Yu, L. Hu, M. Vosgueritchian, H. Wang, X. Xie, J. R. McDonough, X. Cui, Y. Cui, Z. Bao, *Nano Lett.* **2011**, *11*, 2905.
[27] G. Sun, X. Zhang, R. Lin, J. Yang, H. Zhang, P. Chen, *Angew. Chem. Int. Ed.* **2015**, *127*, 4734.
[28] J. Wang, D. Chao, J. Liu, L. Li, L. Lai, J. Lin, Z. Shen, *Nano Energy* **2014**, *7*, 151.
[29] C. Hao, F. Wen, J. Xiang, L. Wang, H. Hou, Z. Su, W. Hu, Z. Liu, *Adv. Funct. Mater.* **2014**, *24*, 6700.
[30] F. Zhou, S. Xin, H. W. Liang, L. T. Song, S. H. Yu, *Angew. Chem. Int. Ed.* **2014**, *53*, 11552.
[31] J. Xiao, D. Choi, L. Cosimbescu, P. Koech, J. Liu, J. P. Lemmon, *Chem. Mater.* **2010**, *22*, 4522.
[32] S. D. Lacey, J. Wan, A. V. W. Cresce, S. M. Russell, J. Dai, W. Bao, K. Xu, L. Hu, *Nano Lett.* **2015**, *15*, 1018.
[33] M. Wang, G. Li, H. Xu, Y. Qian, J. Yang, *ACS Appl. Mater. Interfaces* **2013**, *5*, 1003.
[34] F. Gao, Y.-k. Zhang, X.-d. Wang, *Chin. J. Polym. Sci.* **2010**, *28*, 667.
[35] J. Zhu, W. Sun, D. Yang, Y. Zhang, H. H. Hoon, H. Zhang, Q. Yan, *Small* **2015**, *11*, 4123.
[36] Y. Chen, B. Song, X. Tang, L. Lu, J. Xue, *Small* **2014**, *10*, 1536.
[37] C. Zhu, Z. Zeng, H. Li, F. Li, C. Fan, H. Zhang, *J. Am. Chem. Soc.* **2013**, *135*, 5998.
[38] Z. Gholamvand, D. McAteer, A. Harvey, C. Backes, J. N. Coleman, *Chem. Mater.* **2016**.
[39] D. Zhang, J. Yang, Y. Li, *Small* **2013**, *9*, 1284.
[40] S. Zhao, H. Yin, L. Du, L. He, K. Zhao, L. Chang, G. Yin, H. Zhao, S. Liu, Z. Tang, *ACS Nano* **2014**, *8*, 12660.
[41] J. N. Coleman, M. Lotya, A. O'Neill, S. D. Bergin, P. J. King, U. Khan, K. Young, A. Gaucher, S. De, R. J. Smith, *Science* **2011**, *331*, 568.
[42] A. Ciesielski, P. Samorì, *Chem. Soc. Rev.* **2014**, *43*, 381.
[43] Y. Hernandez, V. Nicolosi, M. Lotya, F. M. Blighe, Z. Sun, S. De, I. McGovern, B. Holland, M. Byrne, Y. K. Gun'Ko, *Nat. Nanotechnol.* **2008**, *3*, 563.
[44] G. Cunningham, M. Lotya, C. S. Cucinotta, S. Sanvito, S. D. Bergin, R. Menzel, M. S. Shaffer, J. N. Coleman, *ACS Nano* **2012**, *6*, 3468.
[45] J. Wu, M. Liu, K. Chatterjee, K. P. Hackenberg, J. Shen, X. Zou, Y. Yan, J. Gu, Y. Yang, J. Lou, *Adv. Mater. Interfaces* **2016**, *3*, 1500669.
[46] Z. Ding, B. Yao, J. Feng, J. Zhang, *J. Mater. Chem. A* **2013**, *1*, 11200.
[47] K. Chang, W. Chen, L. Ma, H. Li, H. Li, F. Huang, Z. Xu, Q. Zhang, J.-Y. Lee, *J. Mater. Chem.* **2011**, *21*, 6251.
[48] H. Chaudhari, D. Kelkar, *Polym. Int.* **1997**, *42*, 380.
[49] K. Wang, X. Zhang, C. Li, H. Zhang, X. Sun, N. Xu, Y. Ma, *J. Mater. Chem.* **2014**, *2*, 19726.
[50] C. Lee, H. Yan, L. E. Brus, T. F. Heinz, J. Hone, S. Ryu, *ACS Nano* **2010**, *4*, 2695.
[51] H. Li, Q. Zhang, C. C. R. Yap, B. K. Tay, T. H. T. Edwin, A. Olivier, D. Baillargeat, *Adv. Funct. Mater.* **2012**, *22*, 1385.
[52] G. Plechinger, S. Heydrich, J. Eroms, D. Weiss, T. Korn, *App. Phys. Lett.* **2012**, *101*, 101906.
[53] G. S. Bang, K. W. Nam, J. Y. Kim, J. Shin, J. W. Choi, S.-Y. Choi, *ACS Appl. Mater. Interfaces* **2014**, *6*, 7084.
[54] M. Viršek, M. Krause, A. Kolitsch, A. Mrzel, I. Iskra, S. O. D. Škapin, M. Remškar, *J. Phys. Chem. C* **2010**, *114*, 6458.
[55] M. Cochet, G. Louarn, S. Quillard, J. Buisson, S. Lefrant, *J. Raman Spectrosc.* **2000**, *31*, 1041.
[56] M. Tagowska, B. Pałys, K. Jackowska, *Synth. Met.* **2004**, *142*, 223.
[57] T.-M. Wu, H.-L. Chang, Y.-W. Lin, *Compos. Sci. Technol.* **2009**, *69*, 639.
[58] J. Fan, M. Wan, D. Zhu, B. Chang, Z. Pan, S. Xie, *J. Appl. Polym. Sci.* **1999**, *74*, 2605.
[59] G. Han, J. Yuan, G. Shi, F. Wei, *Thin Solid Films* **2005**, *474*, 64.
[60] G. Ma, H. Peng, J. Mu, H. Huang, X. Zhou, Z. Lei, *J. Power Sources* **2013**, *229*, 72.
[61] Y. Hwang, H. Sohn, A. Phan, O. M. Yaghi, R. N. Candler, *Nano Lett.* **2013**, *13*, 5271.
[62] H. Zhang, G. Cao, W. Wang, K. Yuan, B. Xu, W. Zhang, J. Cheng, Y. Yang, *Electrochim. Acta* **2009**, *54*, 1153.
[63] K. Chang, W. Chen, *Chem. Commun.* **2011**, *47*, 4252.
[64] X. Yu, M. S. Prévot, K. Sivula, *Chem. Mater.* **2014**, *26*, 5892.
[65] G. Wang, B. Wang, X. Wang, J. Park, S. Dou, H. Ahn, K. Kim, *J. Mater. Chem.* **2009**, *19*, 8378.
[66] X. Zou, J. Wang, C. H. Chiu, Y. Wu, X. Xiao, C. Jiang, W. W. Wu, L. Mai, T. Chen, J. Li, *Adv. Mater.* **2014**, *26*, 6255.
[67] H. Yin, S. Zhao, J. Wan, H. Tang, L. Chang, L. He, H. Zhao, Y. Gao, Z. Tang, *Adv. Mater.* **2013**, *25*, 6270.
[68] T. Liu, L. Finn, M. Yu, H. Wang, T. Zhai, X. Lu, Y. Tong, Y. Li, *Nano Lett.* **2014**, *14*, 2522.
[69] Y. Song, T. Y. Liu, X. X. Xu, D. Y. Feng, Y. Li, X. X. Liu, *Adv. Funct. Mater.* **2015**, *25*, 4626.
[70] A. W. Thornton, S. A. Furman, K. M. Nairn, A. J. Hill, J. M. Hill, M. R. Hill, *Microporous Mesoporous Mater.* **2013**, *167*, 188.
[71] Z. Wang, P. Tammela, P. Zhang, M. Stromme, L. Nyholm, *J. Mater. Chem.* **2014**, *2*, 16761.
[72] C. Backes, N. C. Berner, X. Chen, P. Lafargue, P. LaPlace, M. Freeley, G. S. Duesberg, J. N. Coleman, A. R. McDonald, *Angew. Chem. Int. Ed.* **2015**, *54*, 2638.
[73] R. J. Smith, P. J. King, M. Lotya, C. Wirtz, U. Khan, S. De, A. O'Neill, G. S. Duesberg, J. C. Grunlan, G. Moriarty, *Adv. Mater.* **2011**, *23*, 3944.